nature communications

Article

https://doi.org/10.1038/s41467-026-75130-5

Critical slowing down of semiarid vegetation resilience is amplified by intensifying heatwaves

Received: 11 July 2025

Accepted: 23 June 2026

Published online: 03 July 2026

Check for updates

Li Fu[1,2], Jianping Huang[2] ✉, Changyu Li[2], Wenmin Wei[3], Ming Peng[3], Guolong Zhang[2], Yu Ren[3] & Jianming Deng[1]

Critical slowing down is commonly used as an early-warning signature of declining ecosystem resilience. While widespread greening has been documented, vegetation resilience in semiarid regions has received limited attention, and how climate extremes influence this association remains poorly understood. Here, we quantify vegetation resilience by estimating lag-1 temporal autocorrelation derived from complementary satellite vegetation metrics across global semiarid regions. We find that 56.6% of semiarid vegetated area shows increasing lag-1 temporal autocorrelation, and the spatial mean lag-1 temporal autocorrelation exhibits a sustained upward trend during 2001–2024, indicating declining resilience. Using a quadrant framework, 47.5% of vegetated area is classified as greening concurrent with declining resilience, exceeding the 33.8% showing greening with increasing resilience. Moreover, heatwaves intensified, and precipitation declined, with trend magnitudes and land-cover composition varying among greening–resilience quadrants. Spatial error models indicate that increases in maximum heatwave intensity are more strongly associated with declining resilience under drying trends, whereas this association weakens under wetting. Within-quadrant analyses further characterize conditional associations, consistent with greening–resilience decoupling under hot–dry intensification. Our findings suggest that greening can mask declining resilience, underscoring the need to integrate resilience diagnostics into routine greenness monitoring as climate extremes intensify.

Satellite observations have documented widespread increases in remotely sensed vegetation indices, commonly referred to as greening[1], that have continued through 2024[2]. However, greenness trends do not unambiguously indicate ecosystem improvement. Extreme climatic events have markedly reduced vegetation greenness in many regions[2,3], and evidence indicates that global greening has recently begun to level off[4] and may reverse in certain areas[5,6]. These complexities suggest that assessments of vegetation dynamics focused solely on monotonic changes in canopy greenness and structure may overlook how vegetation systems withstand disturbance and recover thereafter. Apparent greening trends may therefore mask underlying vulnerability, highlighting the need for resilience-focused diagnostics that characterize recovery dynamics and ecosystem stability.

[1]State Key Laboratory of Herbage Improvement and Grassland Agro-Ecosystems, College of Ecology, Lanzhou University, Lanzhou, China. [2]Collaborative Innovation Center for Western Ecological Safety, Lanzhou University, Lanzhou, China. [3]Key Laboratory for Semi-Arid Climate Change of the Ministry of Education, College of Atmospheric Sciences, Lanzhou University, Lanzhou, China. ✉e-mail: hjp@lzu.edu.cn

Critical slowing down (CSD) is widely regarded as an early-warning signature of declining ecosystem resilience, whereby recovery from small perturbations progressively slows as systems approach a critical transition[7] (Supplementary Fig. 1). This slowdown makes anomalies persist longer, increasing similarity between consecutive observations (i.e., stronger temporal persistence) and thereby elevating lag-1 temporal autocorrelation (TAC)[8]. Accordingly, we use lag-1 TAC as a theoretically grounded indicator of CSD and a proxy for inferring changes in vegetation resilience[9,10]. Consistent with this framework, mounting evidence indicates that resilience is declining across multiple regions and biomes[10–13], with particularly pronounced losses reported in climate-sensitive ecosystems such as the Amazon rainforest[9,14,15]. Such resilience decline manifests as slower recovery from climatic and environmental stresses, including droughts, wildfires, and temperature extremes[16,17].

Although previous studies have investigated vegetation resilience in relation to mean climate conditions and variability in temperature and precipitation[11,13,18], the influence of climate extremes, particularly heatwaves, remains insufficiently explored. Heatwaves impose acute thermal stress, often accompanied by elevated vapor pressure deficit (VPD), which can suppress photosynthesis and vegetation growth[19], thereby slowing recovery dynamics and undermining ecosystem stability. With ongoing warming, heatwaves are becoming more frequent, more intense, and longer-lasting, and these trends are projected to continue under future climate scenarios[20]. A series of extreme heatwave events across Europe[21], Australia[22], North America[23], and China[24] underscores the growing potential for widespread ecosystem disruption. Gaining mechanistic insight into how heatwave characteristics shape vegetation resilience is therefore essential for diagnosing ecosystem vulnerability, without conflating greening with improved ecosystem stability.

Semiarid regions ($0.20 \le AI < 0.50$) constitute a major component of global drylands and are especially vulnerable to climate change (Fig. 1h). These regions face escalating pressures from water scarcity, ecological fragility, and desertification risk[25], and they have accounted for more than half of recent global dryland expansion[26]. Moreover, vegetation resilience is strongly constrained by water availability and interannual precipitation variability[27,28]. Heatwaves often coincide with drought and can be particularly severe in drylands compared with humid regions[29], while heatwave risk and frequency are elevated in water-limited environments[30]. Importantly, greening in these regions can reflect structural or compositional shifts, such as shrub or woody encroachment, that elevate satellite-derived vegetation indices but may signal land degradation rather than improvement[31]. Given their ecological fragility and central role in restoration and afforestation initiatives[32], clarifying resilience change in semiarid ecosystems is critical.

In this study, we propose a resilience-based perspective to examine semiarid vegetation responses to intensifying heatwaves and their relationship with greening trends, complementing conventional greening assessments. We then test whether heatwave characteristics are associated with indicators of critical slowing down in ways that depend on background hydroclimatic conditions. To achieve this, we quantify vegetation resilience using lag-1 TAC derived from multiple vegetation indicators, including solar-induced chlorophyll fluorescence (SIF), leaf area index (LAI), and normalized difference vegetation index (NDVI). We then construct a quadrant framework to classify greening–resilience regimes. Building on this, we estimate the effects of heatwave characteristics on vegetation resilience employing a spatial error model that accounts for residual spatial autocorrelation, while incorporating precipitation trends to represent background hydroclimatic conditions (see Methods). Doing so is particularly valuable for disentangling the relationship between greening and resilience, providing a nuanced understanding of semiarid ecosystem resilience under intensifying heatwaves.

Results

Declining vegetation resilience despite greening

Using lag-1 temporal autocorrelation (TAC) of solar-induced chlorophyll fluorescence (SIF) as an early-warning indicator, we detected widespread critical slowing down across global semiarid regions during 2001–2024. Spatially, 56.6% of semiarid vegetated areas showed increasing SIF lag-1 TAC (trend = 0.0016 yr^{-1}), consistent with declining resilience (Fig. 1a, b). This signal is robust to the choice of sliding-window length: estimates from 3-year and 7-year windows yielded spatial patterns consistent with the 5-year baseline (Supplementary Figs. 3–4). Moreover, NDVI- and LAI-based analyses showed consistently positive trends in lag-1 TAC (Supplementary Figs. 5–6), in line with the SIF-based results. NDVI and LAI primarily characterize canopy greenness and structure, whereas SIF is more directly linked to photosynthetic physiology[33] and is sensitive to plant physiological stress under water limitation and heat extremes[34,35]. Given that SIF, NDVI, and LAI capture complementary aspects of vegetation functioning, their agreement reinforces the inference of resilience decline. Furthermore, mean SIF lag-1 TAC increases over time (Fig. 1c, f), while mean SIF showed a sustained upward trend (Fig. 1f), highlighting a mismatch between greening and declining resilience. Over the same period, 78.4% of vegetated areas exhibited positive SIF trends (Supplementary Fig. 7a), with consistent greening patterns also observed in NDVI and LAI (Supplementary Fig. 7b, c). The greening–resilience mismatch is also evident across land-cover types: both SIF and lag-1 TAC trends were generally positive, yet lag-1 TAC increased most strongly in deciduous forests, followed by savannas and closed shrublands, whereas grasslands exhibited comparatively weaker trends (Fig. 1e). Regionally, lag-1 TAC increases were more pronounced in SAM and SAS and weaker in AUS and SAF (Fig. 1d, h; Supplementary Fig. 8), whereas SIF trends remained positive in all nine subregions (Supplementary Fig. 9).

Against the backdrop of widespread greening, we quantified how greening and browning relate to concurrent resilience changes by applying a quadrant-based framework that jointly classifies trends in SIF and SIF lag-1 TAC (Fig. 2). This bivariate scheme partitions the semiarid domain into four quadrants defined by combinations of greening versus browning and resilience decline versus increase. Nearly half of vegetated areas (47.5%) were classified as greening with declining resilience (Quadrant 1), exceeding the fraction exhibiting greening with resilience increases (33.8%; Quadrant 4) (Fig. 2b). Quadrant 1 and Quadrant 4 were often spatially adjacent, reflecting the close juxtaposition of greening areas with divergent resilience trajectories (Fig. 2a). Browning regimes occupied smaller fractions of the semiarid domain, with 10.5% of vegetated areas showing browning and declining resilience (Quadrant 2) and 8.2% showing browning and increasing resilience (Quadrant 3) (Fig. 2b).

Additionally, we evaluated whether resilience decline is more likely under greening than under browning using a conditional-probability difference (Δ), where negative Δ indicates that resilience decline is more likely under greening than under browning. Resilience decline was more likely under greening in AUS, NAF, EU, and NAM, whereas it was more likely under browning in SAM (Fig. 2c). Similar patterns were evident across land-cover types, with open shrublands and grasslands exhibiting a stronger tendency toward resilience decline under greening (Supplementary Fig. 10). Consistently, quadrant composition varies markedly among subregions (Supplementary Fig. 11), with Quadrant 1 exceeding Quadrant 4 in SAS, NAF, and NAM, whereas Quadrant 2 was concentrated in SAM. Taken together, these results indicate that greening was accompanied by declining resilience in global semiarid regions.

Heatwave and precipitation contrasts across greening–resilience regimes

Heatwave counts increased from 2001 to 2024 across global semiarid regions, indicating progressively more frequent heat extremes

https://doi.org/10.1038/s41467-026-75130-5

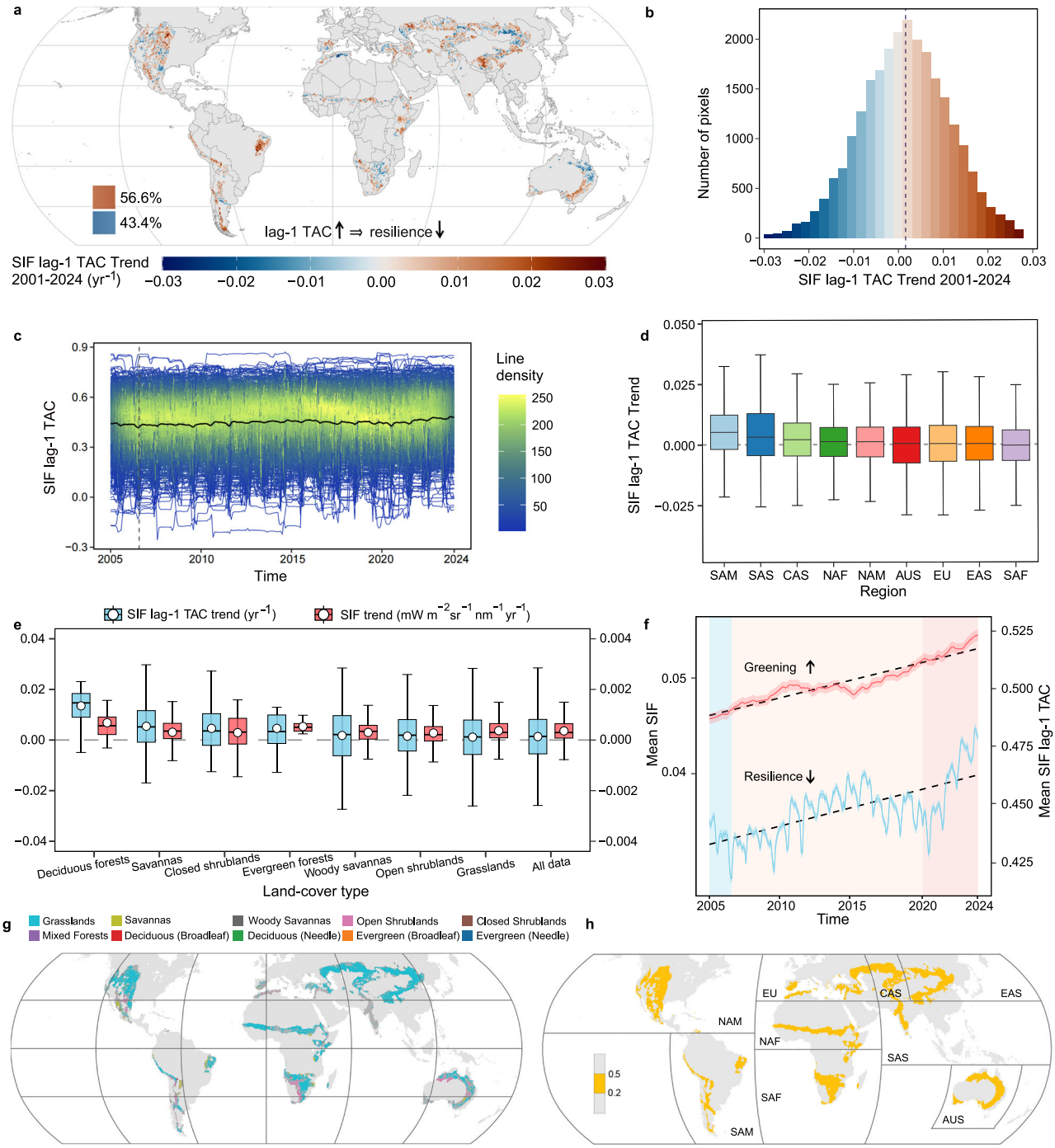


Fig. 1 | General trends in vegetation resilience and greening across global semiarid regions (0.20 ≤ AI < 0.50) during 2001–2024. a Spatial distribution of trends in SIF lag-1 temporal autocorrelation (TAC); positive (negative) trends indicate declining (increasing) resilience. **b** Frequency distribution of SIF lag-1 TAC trends, with the dashed line denoting the area-weighted mean. **c** Time series of mean SIF lag-1 TAC (black line) from December 2005 to December 2024, with the density of lag-1 TAC values for 1000 random pixels shown from dark green to yellow (density values ranging between 1 and 250). The lowest mean lag-1 TAC occurs in July 2007 (dotted vertical line). **d** Boxplots of SIF lag-1 TAC trends across nine subregions. **e** Boxplots show trends in SIF lag-1 TAC (blue; resilience indicator) and SIF (pink; greening indicator) across land-cover types. In d and e, the centre line denotes the median, boxes indicate the 25th and 75th percentiles, whiskers indicate the non-outlier range, and outliers are not shown. The unit of analysis is a valid semiarid vegetated grid cell. In e, hollow dots denote area-weighted means. **f** Temporal evolution of mean SIF (pink line) and mean SIF lag-1 TAC (blue line), with shaded 95% confidence intervals. For comparison, mean SIF is calculated using the same 5-year right-aligned sliding window as lag-1 TAC and plotted at the end of each window. Dashed lines indicate linear trends in the time series. **g** Spatial distribution of stable natural vegetation (IGBP classes 1–10) during 2001–2024. **h** Semiarid study domain and nine subregions: South America (SAM), North America (NAM), Europe (EU), East Asia (EAS), Central Asia (CAS), South Asia (SAS), North Africa (NAF), Southern Africa (SAF), and Australia (AUS).

(Fig. 3a1). Heatwave duration, cumulative intensity, and maximum intensity exhibited nonlinear upward trends (Fig. 3a2–a4), reflecting an increasing heat burden, with a pronounced peak in 2011 that coincided with severe regional heat extremes reported for that period[36,37]. Meanwhile, annual precipitation increased initially and then declined steadily, resulting in an overall drying tendency (Fig. 3a5). This co-occurrence aligns with evidence for increasing compound hot–dry extremes[38,39]. Similar nonlinear temporal evolutions were observed

https://doi.org/10.1038/s41467-026-75130-5

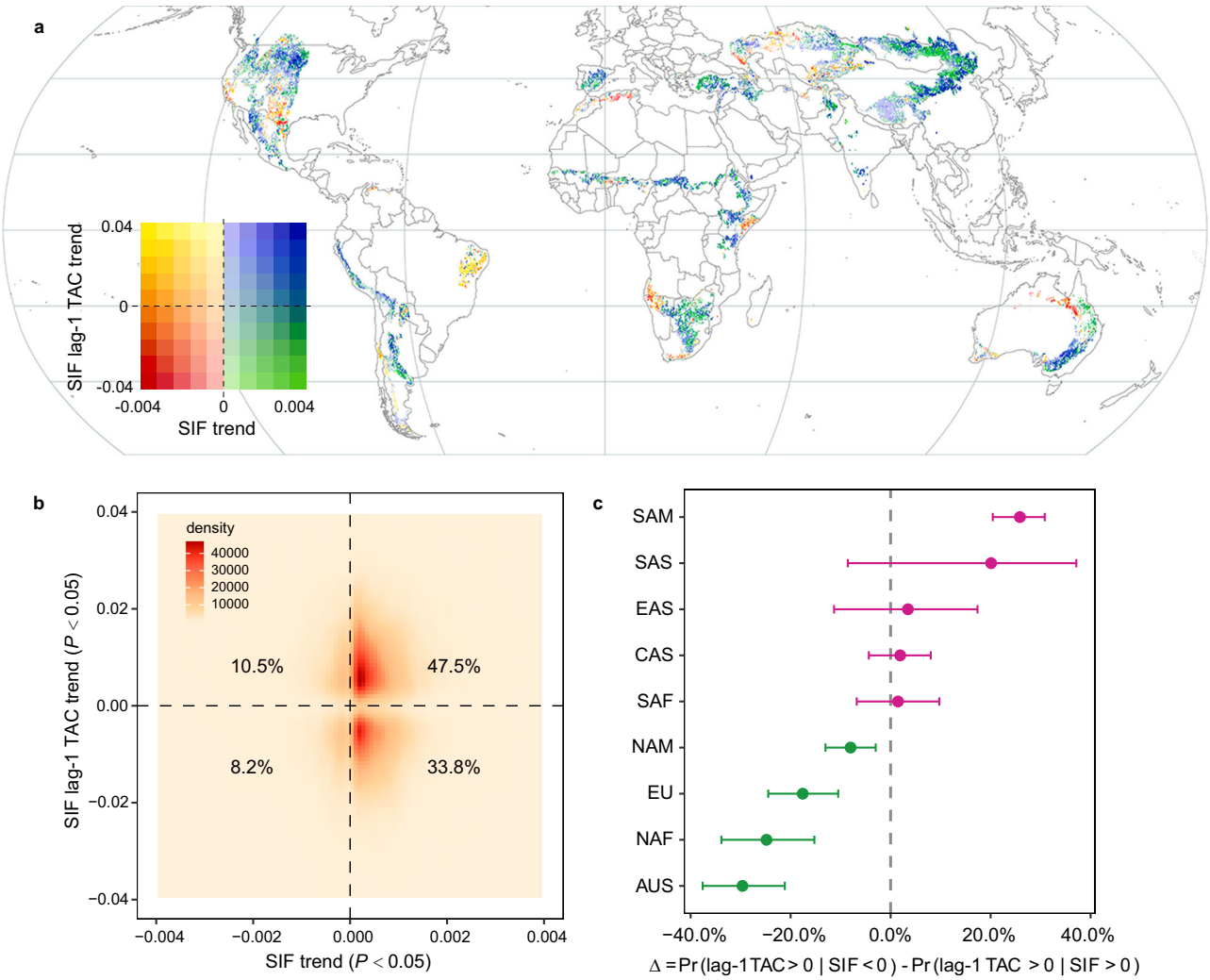


Fig. 2 | Bivariate analysis of vegetation greening and resilience changes across global semiarid regions during 2001–2024. a Spatial distribution of bivariate trends in SIF and SIF lag-1 TAC. Greening (browning) is defined as SIF trend > 0 (< 0), and declining (increasing) resilience is defined as lag-1 TAC trend > 0 (< 0). The legend shows joint quantiles of SIF trends (x-axis; −0.004 to 0.004 $mW{\cdot}m^{-2}{\cdot}sr^{-1}{\cdot}nm^{-1}{\cdot}yr^{-1}$) and SIF lag-1 TAC trends (y-axis; −0.04 to 0.04 yr^{-1}); dashed lines indicate zero. **b** Kernel density of SIF trends and lag-1 TAC trends. Pixels with non-significant trends were excluded ($P > 0.05$). Statistical significance of each linear trend was assessed using two-sided t tests of the regression slope. Numbers indicate the area-weighted percentage of pixels in each quadrant: Quadrant 1 represents greening and declining resilience (SIF trend > 0 and lag-1 TAC trend > 0, 47.5%), Quadrant 2 represents browning and declining resilience (SIF trend < 0 and lag-1 TAC trend > 0, 10.5%), Quadrant 3 represents browning and increasing resilience (SIF trend < 0 and lag-1 TAC trend < 0, 8.2%), and Quadrant 4 represents greening and increasing resilience (SIF trend > 0 and lag-1 TAC trend < 0, 33.8%). **c** Forest plot of the conditional-probability difference (Δ) across nine subregions. Here, p_r^{brown} = Pr(lag-1 TAC trend > 0 | SIF trend < 0), and p_r^{green} = Pr(lag-1 TAC trend > 0 | SIF trend > 0); $\Delta = p_r^{brown} - p_r^{green}$. Positive Δ indicates that resilience decline is more likely under browning than under greening, whereas negative Δ indicates that resilience decline is more likely under greening than under browning. Points indicate area-weighted estimates, and error bars indicate two-sided 95% confidence intervals.

across the four greening–resilience quadrants (Supplementary Fig. 12). Quadrant-level comparisons further showed that heatwave metrics increased across all quadrants, but with differing trend magnitudes (Fig. 3b1–b4). Quadrant 2 exhibited the largest increases across heatwave metrics and the most pronounced precipitation decline (Fig. 3b5). Among the two greening quadrants, Quadrant 1 was characterized by stronger heatwave intensification and drying than Quadrant 4 (Fig. 3b1–b5). These climate contrasts persisted when stratifying by resilience-change classes alone (Supplementary Fig. 13).

Land-cover composition varied across greening–resilience quadrants, although all remained grassland-dominated (Fig. 3c). Given that land cover was held constant throughout 2001–2024 (see Methods), these differences represent cross-quadrant contrasts in land-cover composition. Quadrant 4 contained a higher grassland fraction than Quadrant 1 (91.4% vs. 81.1%), while Quadrant 1 had relatively more open shrublands, savannas, and woody savannas. Quadrants 2 and 3 had lower grassland fractions and were comparatively enriched in shrublands and savannas. Moreover, stratifying climate trends by land-cover type reveals clear heterogeneity, with drying strongest in closed shrublands, followed by deciduous forests and savannas (Supplementary Fig. 14), and heatwave intensification most pronounced in shrub-dominated types (Supplementary Fig. 15). A consistent pattern emerges across nine semiarid subregions (Supplementary Table 2), where shrubland- and savanna-enriched subregions (SAM, AUS, and SAF) experienced stronger heatwave intensification and drying than grassland-dominated regions (SAS, CAS, EAS) (Supplementary Fig. 16). Together, the land-cover and subregional analyses reinforced the quadrant-level association between greening–resilience regimes and hot–dry intensification.

https://doi.org/10.1038/s41467-026-75130-5

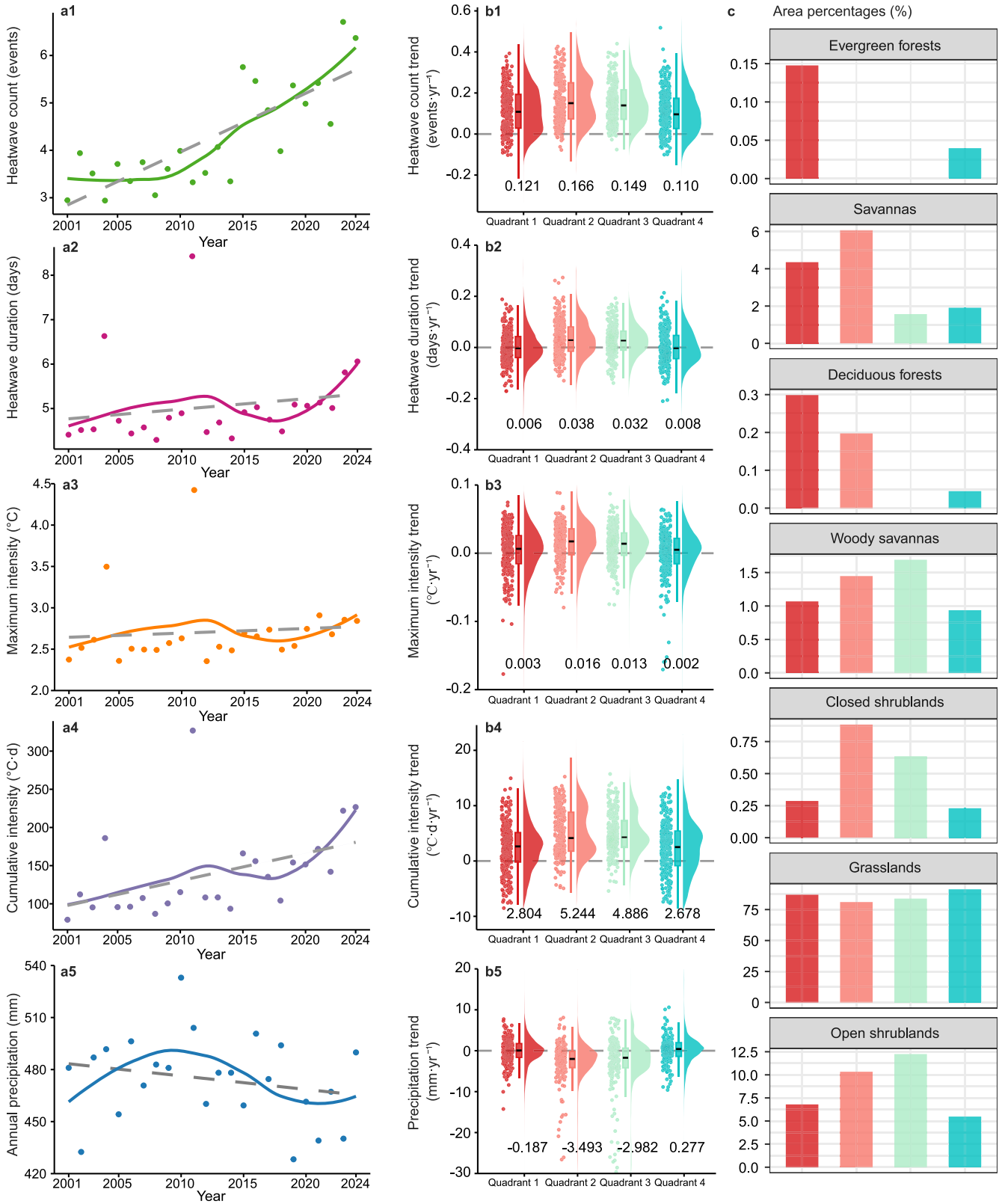


Fig. 3 | Temporal evolution of heatwave characteristics and precipitation, their trends across four greening–resilience quadrants, and land-cover composition in global semiarid regions during 2001–2024. a1–a5 Time series of heatwave count (events), heatwave duration (days), maximum intensity (°C), cumulative intensity (°C·days), and annual precipitation (mm). Solid curves show LOESS-smoothed trajectories of each variable. **b1–b5** Violin plots show the trends in heatwave characteristics and precipitation across the four quadrants (units: events·yr^{-1}, days·yr^{-1}, °C·yr^{-1}, °C·days·yr^{-1}, and mm·yr^{-1}). Colors correspond to the four quadrants defined in Fig. 2. The numbers in each group indicate the area-weighted mean trend for that quadrant. Boxplots show medians, 25th and 75th percentiles, whiskers indicate the non-outlier range, and outliers are not shown. **c** Area-weighted percentages (%) of land-cover types within each quadrant.

https://doi.org/10.1038/s41467-026-75130-5

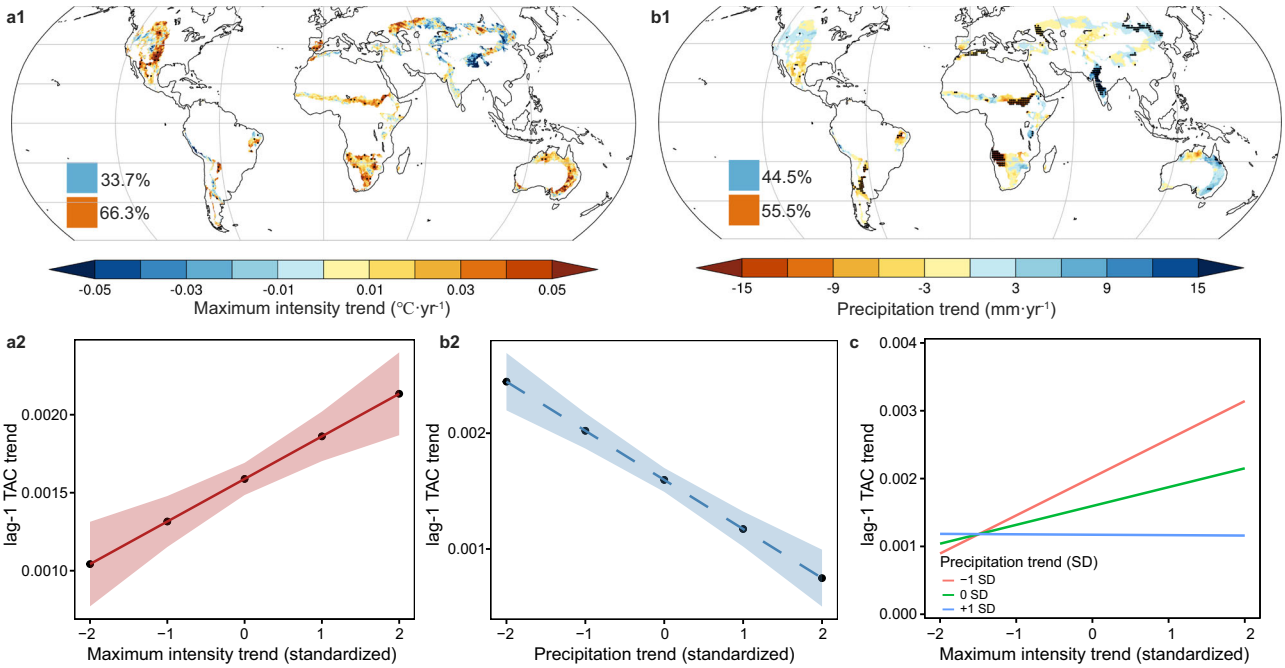


Fig. 4 | Spatial trends in heatwave intensity and precipitation, and their associations with the SIF lag-1 TAC trends. a1 Spatial distribution of the heatwave maximum intensity trend (°C·yr^{-1}) and (**b1**) precipitation trend (mm·yr^{-1}) across global semiarid regions during 2001–2024. Marginal effects represent the predicted change in SIF lag-1 TAC trends when one predictor varies while all other predictors are held at their mean values. **a2** Marginal effect of standardized heatwave maximum intensity trend, and (**b2**) standardized precipitation trend on SIF lag-1 TAC trends, estimated using the spatial error model. Lines indicate model-fitted marginal estimates with other predictors held at their sample means, and shaded bands denote ±1 standard error. **c** Interaction between maximum intensity trend and precipitation trend, showing predicted SIF lag-1 TAC trends as a function of standardized maximum intensity trend at −1, 0, and +1 SD of precipitation trend.

Heatwave extremes amplify resilience decline under drying

To identify climatic drivers of resilience change, we quantified how precipitation trends and heatwave intensification related to trends in SIF lag-1 TAC using spatial error models that account for residual spatial autocorrelation (see Methods). Heatwave intensification was widespread across the semiarid domain, with maximum intensity increasing over 66.3% of the domain (Fig. 4a1). Heatwave frequency and duration also increased, covering 86.5% and 61.2% of the region, respectively (Supplementary Fig. 17a1, b1). Meanwhile, precipitation declined across 55.5% of the domain (Fig. 4b1). Spatial error models indicated lag-1 TAC trends were positively associated with maximum intensity trends (declining resilience), whereas they were negatively associated with precipitation trends (Fig. 4a2, b2). Importantly, maximum intensity interacted with precipitation: the marginal effect of maximum intensity on lag-1 TAC strengthened under drying (−1 SD precipitation trend) but weakened under wetting (+1 SD) (Fig. 4c). In contrast, the marginal effects of heatwave frequency and duration were weaker and less certain (Supplementary Fig. 17a2, b2). Adding an interaction between heatwave frequency and maximum intensity did not improve model fit based on AIC (Supplementary Fig. 18; Supplementary Table 1), supporting the robustness of the retained precipitation–maximum intensity interaction. Overall, these results indicate that drying amplifies the impact of heatwave maximum intensity on resilience decline.

Subsequently, we fitted partial least squares structural equation models (PLS-SEM) within each greening–resilience quadrant to examine multivariate associations among precipitation, heatwave maximum intensity, SIF, and lag-1 TAC trends (Fig. 5). Because quadrants are defined by the signs of SIF and lag-1 TAC trends, the path coefficients represent within-quadrant conditional co-variation rather than causal effects or comparisons of coefficient signs across quadrants. Across quadrants, precipitation trends were positively associated with SIF trends, whereas the associations between precipitation and lag-1 TAC varied by quadrant. The greening quadrants (Q1 and Q4) also differed in their within-quadrant association structures. In Q4, precipitation was negatively associated with lag-1 TAC, whereas maximum intensity was positively associated with lag-1 TAC. In Q1, already classified as greening with declining resilience, maximum intensity covaried positively with SIF but showed a small negative association with lag-1 TAC. Because Q1 is a sign-selected subset with restricted ranges, this coefficient should be interpreted as within-quadrant conditional co-variation, rather than as a comparison with the cross-quadrant spatial error model results. This quadrant is relatively enriched in shrublands and savannas (Fig. 3c), while precipitation showed only weak and non-significant links with lag-1 TAC. In the browning quadrants, maximum intensity was positively associated with lag-1 TAC, with the strongest association in Q3 (Fig. 5). Moreover, within each quadrant, partial correlations between SIF and lag-1 TAC remained weak after controlling for maximum intensity and precipitation, suggesting that their co-variation was largely attributable to climatic covariates rather than a strong direct linkage. Collectively, these quadrant-specific patterns complement the spatial error model result that the positive association between maximum heatwave intensity and lag-1 TAC is stronger under drying, and provide quadrant-level context for the observed greening–resilience divergence (Fig. 6).

Discussion

Despite widespread satellite-observed greening, our analysis reveals that resilience has declined across global semiarid regions, suggesting that greenness gains do not necessarily translate into improved ecosystem stability. We infer resilience changes from lag-1 temporal autocorrelation (TAC), a widely used indicator of critical slowing down (CSD). Rising TAC reflects stronger temporal persistence and slower recovery from perturbations[7]. This greening–resilience decoupling is widespread across semiarid regions and consistent among

https://doi.org/10.1038/s41467-026-75130-5

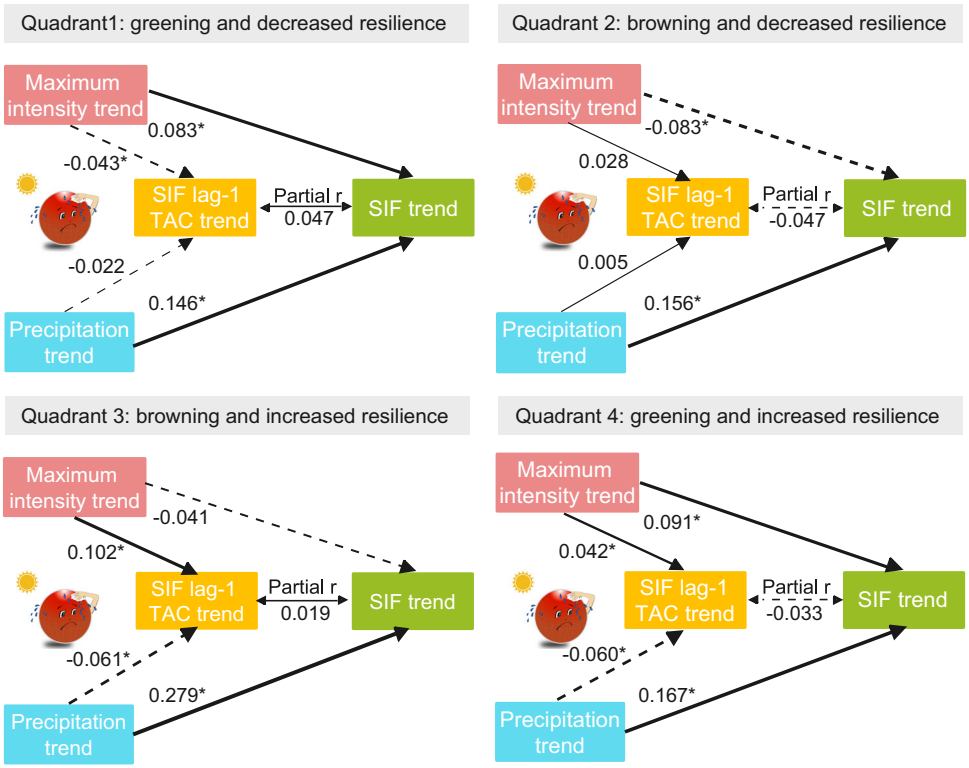


Fig. 5 | Partial least squares structural equation modeling (PLS-SEM) summarizing within-quadrant associations among precipitation trend, heatwave maximum intensity trend, vegetation greening (SIF trend), and resilience (SIF lag-1 TAC trend) across four greening–resilience quadrants (see Fig. 2 for quadrant definitions). Increasing lag-1 TAC is consistent with declining resilience. Solid and dashed lines denote positive and negative standardized path coefficients, and line thickness indicates coefficient magnitude. The dashed bidirectional arrow denotes the partial correlation between SIF lag-1 TAC trend and SIF trend after controlling for precipitation and heatwave maximum intensity trend; path directions do not imply causality. Asterisks indicate paths for which the two-sided 95% bootstrap confidence intervals do not include zero.

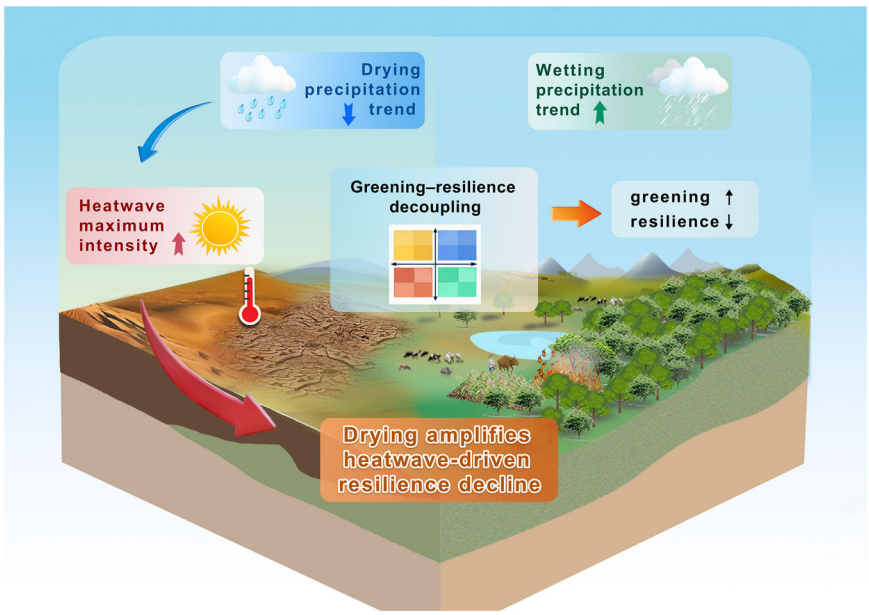


Fig. 6 | Conceptual schematic illustrating the amplifying effect of drying on heatwave-driven resilience decline. The effect of heatwave maximum intensity is amplified under drying trends, whereas it weakens under wetting trends.

complementary satellite indicators, strengthening confidence in our inference.

The quadrant framework further clarifies that similar greening trajectories can correspond to distinct resilience changes, and that these differences align with structured gradients in hydroclimate and land-cover composition. In particular, greening accompanied by declining resilience (Quadrant 1) is more common under warmer and drier conditions and in regions relatively enriched in shrub and savanna components, whereas greening with increased resilience (Quadrant 4) is more characteristic of grassland-dominated systems. This contrast suggests that greening in Quadrant 1 may partly reflect structural or compositional shifts (e.g., shrub or woody encroachment) that elevate satellite greenness metrics without necessarily enhancing recovery dynamics[31,40]. This is compatible with evidence that dryland vegetation metrics differ in their sensitivities to herbaceous versus woody components, such that apparent greening can arise from compositional reorganization rather than uniform functional improvement[41]. Moreover, although woody plants are often drought-tolerant, woody expansion can alter ecosystem water balance and increase transpirational demand, which may constrain post-disturbance recovery under intensifying hot–dry stress[42]. Overall, these considerations reinforce that greening trends should be interpreted alongside community composition, especially in water-limited ecosystems[43].

Importantly, our findings do not contradict established drivers of widespread greenness increases; rather, they refine what greening implies for ecosystem stability. Previous studies have attributed greening to CO_2 fertilization[44] and large-scale land management interventions[45]. Consistent with our findings, decoupling between greening and resilience has been reported in the Amazon rainforest[14], and on the Chinese Loess Plateau[46], where resilience does not increase consistently with greening. Beyond drylands, broader analyses also point to emerging declines in forest resilience under climate change[11]. Our results extend these insights by showing that similar greening trends can mask markedly different resilience trajectories, suggesting that greenness-based assessments alone may overestimate ecosystem improvement. Collectively, these lines of evidence suggest that apparent greenness gains in water-limited ecosystems may mask growing vulnerability, motivating the integration of resilience indicators into early-warning frameworks as climate extremes intensify[47].

A central insight from our analysis is that hydroclimatic background modulates how heatwaves relate to resilience change: the negative association between heatwave maximum intensity and resilience strengthens under drying but weakens under wetting. This pattern suggests that drying acts not only as an independent stressor but also as a key modulator of how heatwaves affect ecosystem resilience. This interpretation is consistent with evidence that water availability and variability are key constraints on vegetation resilience[27], and that wetter conditions can buffer drought legacies and facilitate recovery[48]. Although heatwave frequency and duration have increased, their relationships with resilience are weaker after accounting for spatial structure and drying background, whereas maximum intensity remains the most consistent correlate. This aligns with the view that ecological consequences of climate extremes often hinge on event characteristics, particularly magnitude or peak severity[49]. In this context, higher maximum intensity can impose acute physiological constraints, reducing productivity and generating legacy effects[50]. By contrast, the impacts of less extreme heat stress may be partly buffered by physiological acclimation[51], and repeated exposure can increase leaf thermal tolerance and dampen impacts during subsequent events[52].

This state dependence is consistent with a plausible mechanism whereby precipitation-driven drying may reduce evaporative cooling, increasing temperature extremes[53]. Under such conditions, heat stress can impose stomatal and photosynthetic limitations[54], thereby delaying post-disturbance recovery[55]. In some cases, experiments suggest that drought-stressed plants increase stomatal conductance during heatwaves to cool leaves, accelerating water loss and compounding drought-induced mortality risk[56]. Additionally, greening itself may heighten exposure to hot–dry stress by increasing transpiration demand and accelerating soil-water depletion[57]. Taken together, these patterns suggest that drying may amplify the resilience impacts of heatwaves.

Several limitations merit consideration. First, lag-1 TAC is an indirect proxy for resilience within the CSD framework and can be sensitive to non-stationarity, long-term trends, and changes in the underlying noise structure. To minimize these effects, we performed robustness checks across multiple vegetation indicators and window lengths. Direct and precise measurement of resilience remains challenging because it generally requires controlled disturbance–recovery experiments or waiting for sufficiently large natural perturbations[12]. Accordingly, TAC-based metrics remain widely used in resilience change studies[6,13,36,46]. Second, precipitation trends provide a simple proxy for hydroclimatic drying but cannot capture all dimensions of drought processes; future work could incorporate complementary drought metrics (e.g., SPI, SPEI, and soil moisture) and consider explicit driver–response time lags to better attribute underlying mechanisms.

Our results reveal widespread decoupling between greening and resilience across global semiarid regions, raising concerns about the sustainability of greening trajectories. We further show that the association between heatwave maximum intensity and resilience decline is strongest under drying. Overall, these findings caution against treating greening as a proxy for ecosystem stability and underscore the value of integrating resilience indicators into routine greenness monitoring, particularly because resilience loss can be detectable before declines in greenness become apparent[58]. Such integration offers a practical pathway toward more robust assessments of semiarid ecosystem vulnerability and may help inform targeted conservation and restoration strategies under intensifying compound hot–dry extremes.

Methods

Study domain

Semiarid regions were defined using the Aridity Index (AI), calculated as the ratio of total annual precipitation to potential evapotranspiration (AI = P/PET). We used the AI dataset at 0.5° × 0.5° resolution based on the 1961–1990 climatology[59]. Following the standard UNEP dryland classification, semiarid regions were defined as $0.20 \le AI < 0.50$[26]. Analyses were further restricted to 60°S–60°N to minimize potential high-latitude influences related to snow/ice conditions (Fig. 1h). We used a time-invariant semiarid mask to ensure a consistent study domain across all analyses.

Vegetation indicators

We used three satellite-based vegetation indicators to characterize vegetation resilience, capturing complementary aspects of photosynthetic functioning, canopy greenness, and canopy structure. (i) Solar-induced chlorophyll fluorescence (SIF) was obtained from the monthly GOSIF v2 product at 0.05° spatial resolution[60]. This dataset provides a proxy for photosynthetic activity and is generated using a machine-learning algorithm trained on OCO-2 SIF observations, MODIS surface reflectance, and meteorological reanalysis data. (ii) Normalized difference vegetation index (NDVI) was derived from the MODIS/Terra Vegetation Indices Monthly L3 Global 0.05° CMG product (MOD13C2, Collection 6.1) at 0.05° spatial resolution[61]. Pixels with very low values (NDVI < 0.1) were removed using a vegetation mask based on the 2001–2024 long-term mean NDVI, excluding barren or perennial snow/ice. (iii) Leaf area index (LAI) was derived from the MODIS 6.1 Terra LAI/FPAR 8-day composite product (MOD15A2H) via Google Earth Engine (GEE)[62]. Because MOD15A2H is provided at 500 m

and an 8-day interval, we aggregated it to monthly values by averaging within each month and then regridded it to the ~0.05° analysis grid using bilinear resampling.

Selection of stable, low-disturbance vegetation pixels

To minimize potential confounding from land-cover conversion, we used the annual MODIS MCD12C1 land-cover product (Majority_Land_Cover_Type_1)[63] to identify pixels with stable natural vegetation (IGBP 1–10; including forests, shrublands, savannas, and grasslands, etc.). We retained only pixels whose IGBP class remained identical in every year from 2001 to 2024; pixels exhibiting any class change were treated as converted and excluded. In addition, to further reduce recurrent fire disturbance, we used the GFEDv5 burned-area product over 2002–2022[64] (the latest period available for our analysis) to compute the cumulative burned fraction. We then excluded pixels with cumulative burned fraction above the 95th percentile as high-fire pixels[65]. This filter removes only the most fire-affected pixels rather than restricting the analysis to fire-free conditions. The resulting stable, low-disturbance vegetation mask was applied to all vegetation indicators in subsequent analyses.

Lag-1 temporal autocorrelation

Before estimating lag-1 temporal autocorrelation (TAC) as a proxy for vegetation resilience, monthly vegetation indicators (SIF/NDVI/LAI) were detrended and deseasonalized using STL (Seasonal and Trend decomposition using Loess). STL decomposes a time series into long-term trend, seasonal, and residual components; the residual component was treated as the anomaly series for estimating lag-1 TAC (Supplementary Fig. 2). The decomposition was implemented using the stl() function in the stats package in R v4.3.3[66].

Next, we computed lag-1 TAC using right-aligned rolling windows of 60 months (5 years) as the main analysis[14,27], and repeated the calculation using window lengths of 36 and 84 months (3 and 7 years) as robustness checks. The rolling-window length sets the memory scale of the estimator: shorter windows are more responsive to interannual variability, whereas longer windows further smooth high-frequency fluctuations.

Within each rolling window, lag-1 TAC (ϕ) was quantified as the lag-1 autocorrelation of the anomaly series, which can be expressed as a first-order autoregressive relationship:

$$X_{t+1} = \phi X_t + \varepsilon_t \quad (1)$$

where X_t and X_{t+1} are STL residual anomalies at times t and $t+1$, respectively, ε_t is the error term, and ϕ is lag-1 TAC. Each window-based estimate was assigned to the end month of the corresponding window (right-aligned). Specifically, the estimate assigned to month t is computed from the 60-month window ending at t (e.g., the value at December 2005 is based on January 2001–December 2005).

Changes in vegetation resilience were inferred from the slope of a linear regression fitted to the lag-1 TAC time series. Increasing lag-1 TAC indicates slower recovery from disturbances and declining resilience, whereas decreasing lag-1 TAC indicates increasing resilience[11]. The same lag-1 TAC workflow was applied to NDVI and LAI (Supplementary Figs. 5, 6). Finally, we summarized SIF lag-1 TAC trends for nine regions: Australia (AUS), North America (NAM), South America (SAM), Europe (EU), North Africa (NAF), Southern Africa (SAF), Central Asia (CAS), East Asia (EAS), and South Asia (SAS).

Greening–resilience quadrant framework

To compare temporal changes in vegetation greening and resilience, we calculated spatial mean trajectories of the 60-month right-aligned sliding mean SIF and the corresponding lag-1 TAC time series (Fig. 1f). For each time step, uncertainty in the spatial mean was quantified using a two-sided t-based 95% confidence interval. We estimated the linear trend in the mean SIF series, with a positive (negative) slope indicating greening (browning). By comparing the mean SIF trajectory with the corresponding mean lag-1 TAC over the same period, we assessed whether greening coincided with increasing or declining resilience.

To characterize the joint distribution of greening and resilience changes, we visualized the relationship between SIF trends and SIF lag-1 TAC trends using a two-dimensional kernel density plot (Fig. 2b). Pixels were classified into four greening–resilience quadrants based on the signs of the two trends; only pixels with statistically significant trends in both variables ($P < 0.05$) were included. Specifically, Quadrant 1 represents greening (SIF trend > 0) with declining resilience (lag-1 TAC trend > 0), Quadrant 2 represents browning (SIF trend < 0) with declining resilience, Quadrant 3 represents browning and increasing resilience (lag-1 TAC trend < 0), and Quadrant 4 represents greening with increasing resilience.

Based on this quadrant framework, we further quantified whether resilience decline was more likely under greening or browning using a conditional-probability difference (Fig. 2c). The conditional probability of resilience decline under browning was defined as $p_r^{brown} = \Pr(\text{lag-1 TAC trend} > 0 \mid \text{SIF trend} < 0)$, corresponding to the proportion of pixels in Quadrant 2 among all browning pixels (Quadrants 2 + 3). Likewise, the conditional probability of resilience decline under greening was defined as $p_r^{green} = \Pr(\text{lag-1 TAC trend} > 0 \mid \text{SIF trend} > 0)$, corresponding to the proportion of pixels in Quadrant 1 among all greening pixels (Quadrants 1 + 4). We then calculated the conditional-probability difference as $\Delta = p_r^{brown} - p_r^{green}$, where positive values indicate that resilience decline is more likely under browning than under greening, and negative values indicate the opposite.

Identification and calculation of heatwaves

Heatwaves are prolonged periods of anomalously high temperatures and were defined as periods of at least three consecutive days during which the daily maximum temperature (T_{max}) exceeds the 90th percentile threshold for that calendar day, according to the relative threshold method[67]. The 90th percentile threshold for each calendar day was estimated using a 15-day moving window (±7 days) and daily T_{max} data from the full study period (2001–2024). Daily T_{max} was derived from the ERA5 hourly 2 m air temperature reanalysis dataset as the daily maximum of the hourly values[68]. After identifying heatwaves, we calculated four commonly used annual metrics: heatwave count, heatwave duration, cumulative intensity, and maximum intensity[19]. Among them, heatwave count refers to the number of heatwave events occurring within a given year. Heatwave duration is defined as the average number of consecutive days per heatwave event in a year. Cumulative intensity is defined as the total temperature exceedance above the 90th percentile threshold, summed across all heatwave days in a year. Maximum intensity is defined as the mean of the peak daily temperature exceedances above the threshold recorded in each heatwave event in a year.

Spatial error models

To quantify how trends in heatwave characteristics and precipitation are associated with changes in vegetation resilience, we fitted spatial error models using the errorsarlm function in the R package spatialreg, which implements a simultaneous autoregressive error specification. The trend in SIF lag-1 TAC was used as the response variable, and trends in heatwave count, heatwave duration, maximum intensity, and precipitation were included as explanatory variables. All explanatory variables were standardized (mean = 0, SD = 1) prior to model fitting. To reduce multicollinearity among heatwave metrics, we excluded cumulative intensity because it was strongly collinear with other heatwave metrics; variance inflation factors (VIFs) for the remaining predictors were < 5.

We first fitted an ordinary least squares (OLS) model and assessed spatial dependence in the residuals. A Moran's I test on OLS residuals indicated significant positive spatial autocorrelation. To characterize the spatial dependence structure, we computed an empirical variogram of the standardized OLS residuals and fitted an exponential variogram model. The fitted correlation range (~ 93 km) was used to define a distance-based neighbor list (great-circle distances) and to construct a row-standardized spatial weights matrix W. Second, using the 93-km weight matrix W, we conducted Lagrange multiplier (LM) diagnostics to compare alternative spatial specifications, which favored the spatial error specification. In spatial error models, spatial autocorrelation is captured in the disturbance term rather than through a spatial lag of the response. The model is defined as:

$$y = X\beta + u, u = \lambda \mathrm{W}u + \varepsilon \quad (2)$$

where y is the SIF lag-1 TAC trend, X is the matrix of standardized predictors, W is the spatial weights matrix, β is the vector of regression coefficients, u is a spatially correlated error term, λ is the spatial error parameter, and ε is an independent error term.

Subsequently, we compared candidate spatial error models with identical main effects but alternative interaction terms (Supplementary Table 1). The best-supported model (lowest AIC) included an interaction between heatwave maximum intensity and precipitation trends, and was retained as the main spatial error model: SIF lag-1 TAC ~ heatwave count + heatwave duration + maximum intensity + precipitation trend + (maximum intensity × precipitation trend).

As robustness checks, we refitted the main spatial error model using alternative neighborhood distances (93, 186, and 278 km; representing multiples of the fitted variogram range) and confirmed that the retained interaction term remained negative, with statistical support across specifications. We further tested an additional interaction between heatwave count and maximum intensity (Supplementary Fig. 18), but this interaction did not improve model fit based on AIC.

Partial least squares structural equation modeling (PLS-SEM)

To characterize within-quadrant multivariate associations among heatwaves, greening, and resilience change, we fitted partial least squares structural equation models (PLS-SEM) separately for each greening–resilience quadrant using the plspm package in R v4.3.3. PLS-SEM is a component-based path modeling approach suitable for estimating standardized path coefficients in multivariate systems without strict distributional assumptions[69]. The model included observed variables of heatwave maximum intensity trend, precipitation trend, SIF trend (greening), and SIF lag-1 TAC trend (resilience change). We focused on maximum intensity because it provided the most robust predictor of lag-1 TAC in the spatial error models. All variables were standardized prior to model fitting to ensure comparability of effect sizes. We assessed the stability and significance of path coefficients using 1000 bootstrap resamples. The bidirectional dashed arrow denotes the partial correlation between the SIF trend and the SIF lag-1 TAC trend after controlling for precipitation and maximum intensity trends. Models were fitted independently within each quadrant to avoid cross-quadrant inference and to reflect conditional relationships under the quadrant definitions.

Reporting summary

Further information on research design is available in the Nature Portfolio Reporting Summary linked to this article.

Data availability

All data used in this study are publicly accessible. The solar-induced chlorophyll fluorescence (SIF) data were obtained from the monthly GOSIF v2 product, which is available at http://data.globalecology.unh.edu/data/GOSIF_v2/Monthly/. The normalized difference vegetation index (NDVI) data were from the MODIS/Terra Vegetation Indices Monthly L3 Global 0.05° CMG product (MOD13C2, Collection 6.1), which can be accessed at https://www.earthdata.nasa.gov/data/catalog/lpcloud-mod13c2-061. The leaf area index (LAI) data were obtained from the MODIS 6.1 Terra Leaf Area Index/FPAR 8-day composite product (MOD15A2H), accessed via Google Earth Engine (GEE) and available at https://developers.google.com/earth-engine/datasets/catalog/MODIS_061_MOD15A2H. Monthly precipitation data were from the TerraClimate dataset and available at https://climate.northwestknowledge.net/TERRACLIMATE-DATA. Daily temperatures were derived from the hourly 2 m air temperature data from the ERA5 hourly dataset, which can be obtained from https://cds.climate.copernicus.eu/cdsapp#!/dataset/reanalysis-era5-single-levels?tab=overview. The burned-area data were obtained from the Global Fire Emissions Database (GFEDv5) and can be accessed at https://surfdrive.surf.nl/files/index.php/s/VPMEYinPeHtWVxn?path=%2F. Land-cover data were obtained from the MODIS MCD12C1 (Collection 6.1) product and are available at https://www.earthdata.nasa.gov/data/catalog/lpcloud-mcd12c1-061.

Code availability

The code used to process the datasets and generate the figures has been deposited in Zenodo at https://doi.org/10.5281/zenodo.18797940.

References

1. Piao, S. et al. Characteristics, drivers and feedbacks of global greening. *Nat. Rev. Earth Environ.* **1**, 14–27 (2020).
2. Gui, Y. et al. Vegetation greenness in 2024. *Nat. Rev. Earth Environ.* **6**, 255–257 (2025).
3. Yuan, W. et al. Increased atmospheric vapor pressure deficit reduces global vegetation growth. *Sci. Adv.* **5**, eaax1396 (2019).
4. Winkler, A. J. et al. Slowdown of the greening trend in natural vegetation with further rise in atmospheric CO_2. *Biogeosciences* **18**, 4985–5010 (2021).
5. Feng, X. et al. Recent leveling off of vegetation greenness and primary production reveals the increasing soil water limitations on the greening Earth. *Sci. Bull.* **66**, 1462–1471 (2021).
6. Fu, L. et al. Prevalence of vegetation browning in China's drylands under climate change. *Geogr. Sustain.* **5**, 405–414 (2024).
7. Scheffer, M. et al. Early-warning signals for critical transitions. *Nature* **461**, 53–59 (2009).
8. Dakos, V., van Nes, E. H., d'Odorico, P. & Scheffer, M. Robustness of variance and autocorrelation as indicators of critical slowing down. *Ecology* **93**, 264–271 (2012).
9. Van Passel, J. et al. Critical slowing down of the Amazon forest after increased drought occurrence. *Proc. Natl. Acad. Sci. USA* **121**, e2316924121 (2024).
10. Verbesselt, J. et al. Remotely sensed resilience of tropical forests. *Nat. Clim. Chang.* **6**, 1028–1031 (2016).
11. Forzieri, G., Dakos, V., McDowell, N. G., Ramdane, A. & Cescatti, A. Emerging signals of declining forest resilience under climate change. *Nature* **608**, 534–539 (2022).
12. Smith, T., Traxl, D. & Boers, N. Empirical evidence for recent global shifts in vegetation resilience. *Nat. Clim. Chang.* **12**, 477–484 (2022).
13. Yao, Y. et al. Declined terrestrial ecosystem resilience. *Glob. Change Biol.* **30**, e17291 (2024).
14. Boulton, C. A., Lenton, T. M. & Boers, N. Pronounced loss of Amazon rainforest resilience since the early 2000s. *Nat. Clim. Chang.* **12**, 271–278 (2022).
15. Wang, H. et al. Anthropogenic disturbance exacerbates resilience loss in the Amazon rainforests. *Glob. Change Biol.* **30**, e17006 (2024).

16. Gu, L. et al. Flash drought impacts on global ecosystems amplified by extreme heat. *Nat. Geosci.* **18**, 709–715 (2025).
17. Steel, Z. L. et al. Ecological resilience and vegetation transition in the face of two successive large wildfires. *J. Ecol.* **109**, 3340–3355 (2021).
18. Feng, Y. et al. Reduced resilience of terrestrial ecosystems locally is not reflected on a global scale. *Commun. Earth Environ.* **2**, 88 (2021).
19. Xu, W. et al. Impacts of record-breaking compound heatwave and drought events in 2022 China on vegetation growth. *Agric. Meteorol.* **344**, 109799 (2024).
20. Han, Q., Sun, S., Liu, Z., Xu, W. & Shi, P. Accelerated exacerbation of global extreme heatwaves under warming scenarios. *Int. J. Climatol.* **42**, 5430–5441 (2022).
21. Liu, X., He, B., Guo, L., Huang, L. & Chen, D. Similarities and differences in the mechanisms causing the European summer heatwaves in 2003, 2010, and 2018. *Earth's. Future* **8**, e2019EF001386 (2020).
22. Lewis, S. C. & Karoly, D. J. Anthropogenic contributions to Australia's record summer temperatures of 2013. *Geophys. Res. Lett.* **40**, 3705–3709 (2013).
23. Thompson, V. et al. The 2021 western North America heat wave among the most extreme events ever recorded globally. *Sci. Adv.* **8**, eabm6860 (2022).
24. Hao, Z. et al. The 2022 Sichuan-Chongqing spatio-temporally compound extremes: a bitter taste of novel hazards. *Sci. Bull.* **68**, 1337–1339 (2023).
25. Guan, X. & Huang, J. Constructing semi-arid ecological barriers to prevent desertification. *Innov. Geosci.* **2**, 100067 (2024).
26. Huang, J., Yu, H., Guan, X., Wang, G. & Guo, R. Accelerated dryland expansion under climate change. *Nat. Clim. Chang.* **6**, 166–171 (2016).
27. Smith, T. & Boers, N. Global vegetation resilience linked to water availability and variability. *Nat. Commun.* **14**, 498 (2023).
28. Wang, W. et al. Increasing aridity and interannual precipitation variability drives resilience declines in restored forests across China. *Earth's. Future* **13**, e2025EF006164 (2025).
29. Wang, C. et al. Drought-heatwave compound events are stronger in drylands. *Weather Clim. Extrem.* **42**, 100632 (2023).
30. Wang, C. et al. Changes in global heatwave risk and its drivers over one century. *Earth's. Future* **12**, e2024EF004430 (2024).
31. Saha, M., Scanlon, T. & D'Odorico, P. Examining the linkage between shrub encroachment and recent greening in water-limited southern Africa. *Ecosphere* **6**, 1–16 (2015).
32. Liu, H. et al. Nature-based framework for sustainable afforestation in global drylands under changing climate. *Glob. Change Biol.* **28**, 2202–2220 (2022).
33. Frankenberg, C. et al. New global observations of the terrestrial carbon cycle from GOSAT: patterns of plant fluorescence with gross primary productivity. *Geophys. Res. Lett.* **38**, L17706 (2011).
34. Porcar-Castell, A. et al. Linking chlorophyll a fluorescence to photosynthesis for remote sensing applications: mechanisms and challenges. *J. Exp. Bot.* **65**, 4065–4095 (2014).
35. Sun, Y. et al. Drought onset mechanisms revealed by satellite solar-induced chlorophyll fluorescence: insights from two contrasting extreme events. *J. Geophys. Res. Biogeosci.* **120**, 2427–2440 (2015).
36. Peterson, T. C., Stott, P. A. & Herring, S. Explaining extreme events of 2011 from a climate perspective. *Bull. Am. Meteorol. Soc.* **93**, 1041–1067 (2012).
37. Hoerling, M. et al. Anatomy of an extreme event. *J. Clim.* **26**, 2811–2832 (2013).
38. Mukherjee, S. & Mishra, A. K. Increase in compound drought and heatwaves in a warming world. *Geophys. Res. Lett.* **48**, e2020GL090617 (2021).
39. Yin, J. & Slater, L. Understanding heatwave-drought compound hazards and impacts on socio-ecosystems. *Innov. Geosci.* **1**, 100042 (2023).
40. Deng, Y., Li, X., Shi, F. & Hu, X. Woody plant encroachment enhanced global vegetation greening and ecosystem water-use efficiency. *Glob. Ecol. Biogeogr.* **30**, 2337–2353 (2021).
41. Andela, N., Liu, Y. Y., van Dijk, A. I. J. M., de Jeu, R. A. M. & McVicar, T. R. Global changes in dryland vegetation dynamics (1988–2008) assessed by satellite remote sensing: comparing a new passive microwave vegetation density record with reflective greenness data. *Biogeosciences* **10**, 6657–6676 (2013).
42. Acharya, B. S., Kharel, G., Zou, C. B., Wilcox, B. P. & Halihan, T. Woody plant encroachment impacts on groundwater recharge: a review. *Water* **10**, 1466 (2018).
43. Cao, X., Liu, Y., Cui, X., Chen, J. & Chen, X. Mechanisms, monitoring and modeling of shrub encroachment into grassland: a review. *Int. J. Digit. Earth* **12**, 625–641 (2019).
44. Zhu, Z. et al. Greening of the Earth and its drivers. *Nat. Clim. Chang.* **6**, 791–795 (2016).
45. Chen, C. et al. China and India lead in greening of the world through land-use management. *Nat. Sustain.* **2**, 122–129 (2019).
46. Wang, Z. et al. Vegetation resilience does not increase consistently with greening in China's loess plateau. *Commun. Earth Environ.* **4**, 336 (2023).
47. Nijp, J. J. et al. Spatial early warning signals for impending regime shifts: a practical framework for application in real-world landscapes. *Glob. Change Biol.* **25**, 1905–1921 (2019).
48. Jiang, P. et al. Enhanced growth after extreme wetness compensates for post-drought carbon loss in dry forests. *Nat. Commun.* **10**, 195 (2019).
49. Smith, M. D. An ecological perspective on extreme climatic events: a synthetic definition and framework to guide future research. *J. Ecol.* **99**, 656–663 (2011).
50. Bastos, A. et al. Direct and seasonal legacy effects of the 2018 heat wave and drought on European ecosystem productivity. *Sci. Adv.* **6**, eaba2724 (2020).
51. Nievola, C. C., Carvalho, C. P., Carvalho, V. & Rodrigues, E. Rapid responses of plants to temperature changes. *Temperature* **4**, 371–405 (2017).
52. Ahrens, C. W. et al. Repeated extreme heatwaves result in higher leaf thermal tolerances and greater safety margins. *N. Phytol.* **232**, 1212–1225 (2021).
53. Berg, A. et al. Impact of soil moisture–atmosphere interactions on surface temperature distribution. *J. Clim.* **27**, 7976–7993 (2014).
54. Breshears, D. D. et al. Underappreciated plant vulnerabilities to heat waves. *N. Phytol.* **231**, 32–39 (2021).
55. Yao, Y. et al. Compound hot–dry events greatly prolong the recovery time of dryland ecosystems. *Natl. Sci. Rev.* **11**, nwae274 (2024).
56. Marchin, R. M. et al. Extreme heat increases stomatal conductance and drought-induced mortality risk in vulnerable plant species. *Glob. Change Biol.* **28**, 1133–1146 (2022).
57. Li, J. et al. Future increase in compound soil drought-heat extremes exacerbated by vegetation greening. *Nat. Commun.* **15**, 10875 (2024).
58. Liu, Y., Kumar, M., Katul, G. G. & Porporato, A. Reduced resilience as an early warning signal of forest mortality. *Nat. Clim. Chang.* **9**, 880–885 (2019).
59. Feng, S. & Fu, Q. Expansion of global drylands under a warming climate. *Atmos. Chem. Phys.* **13**, 10081–10094 (2013).
60. Li, X. & Xiao, J. A global, 0.05-degree product of solar-induced chlorophyll fluorescence derived from OCO-2, MODIS, and reanalysis data. *Remote Sens.* **11**, 517 (2019).
61. Didan, K. MODIS/Terra Vegetation Indices Monthly L3 Global 0.05Deg CMG V061. NASA EOSDIS Land Processes DAAC (2021).

62. Myneni, R., Knyazikhin, Y. & Park, T. MODIS/Terra Leaf Area Index/FPAR 8-day L4 Global 500 m SIN Grid V061. NASA EOSDIS Land Processes *DAAC* (2021).
63. Friedl, M. & Sulla-Menashe, D. MODIS/Terra+Aqua Land Cover Type Yearly L3 Global 0.05Deg CMG V061. NASA EOSDIS Land Processes DAAC (2022).
64. Chen, Y. et al. Multi-decadal trends and variability in burned area from the fifth version of the Global Fire Emissions Database (GFED5). *Earth Syst. Sci. Data* **15**, 5227–5259 (2023).
65. Guo, Z. et al. Reconstructed global monthly burned area maps from 1901 to 2020. *Earth Syst. Sci. Data* **17**, 3599–3618 (2025).
66. R Core Team. *R:* A language and environment for statistical computing. R Foundation for Statistical Computing, Vienna, Austria (2024).
67. Perkins-Kirkpatrick, S. E. & Lewis, S. C. Increasing trends in regional heatwaves. *Nat. Commun.* **11**, 3357 (2020).
68. Hersbach, H. et al. The ERA5 global reanalysis. *Q.J.R. Meteorol. Soc.* **146**, 1999–2049 (2020).
69. Zhong, Z. et al. Disentangling the effects of vapor pressure deficit on northern terrestrial vegetation productivity. *Sci. Adv.* **9**, eadf3166 (2023).

Author contributions

L.F. and J.H. conceived and designed the study. L.F. and C.L. performed the data analyses. L.F. prepared the figures and wrote the initial draft. W.W., M.P., G.Z., and Y.R. contributed to the result interpretation. J.D. contributed to manuscript revision. All authors reviewed and approved the manuscript.

Funding

This work was supported by the Fundamental and Interdisciplinary Disciplines Breakthrough Plan of the Ministry of Education of China (JYB2025XDXM910 to J.H.), the National Natural Science Foundation of China (32225032 to J.D.), the National Key Research and Development Program of China (2023YFF0805602 to J.D.), the China Postdoctoral Science Foundation (2025M782643 to L.F.), the Lanzhou Special Fund for Talent Program awarded to J.H., and the 111 Project (B25040 to J.H.).

Competing interests

The authors declare no competing interests.

Additional information

Supplementary information The online version contains supplementary material available at https://doi.org/10.1038/s41467-026-75130-5.

Correspondence and requests for materials should be addressed to Jianping Huang.

Peer review information *Nature Communications* thanks Jane Southworth and the other, anonymous, reviewer(s) for their contribution to the peer review of this work. A peer review file is available.

Reprints and permissions information is available at http://www.nature.com/reprints

Publisher's note Springer Nature remains neutral with regard to jurisdictional claims in published maps and institutional affiliations.

Open Access This article is licensed under a Creative Commons Attribution-NonCommercial-NoDerivatives 4.0 International License, which permits any non-commercial use, sharing, distribution and reproduction in any medium or format, as long as you give appropriate credit to the original author(s) and the source, provide a link to the Creative Commons licence, and indicate if you modified the licensed material. You do not have permission under this licence to share adapted material derived from this article or parts of it. The images or other third party material in this article are included in the article's Creative Commons licence, unless indicated otherwise in a credit line to the material. If material is not included in the article's Creative Commons licence and your intended use is not permitted by statutory regulation or exceeds the permitted use, you will need to obtain permission directly from the copyright holder. To view a copy of this licence, visit http://creativecommons.org/licenses/by-nc-nd/4.0/.

© The Author(s) 2026